A digitally programmable 3D microenvironment directs satellite cell function

Shudong Zhao, Lei Wu, Sara Taiyari, Huiliang Li, Jianfei Sun, Jishizhan Chen,
Wenhui Song, Massimiliano Cerletti

PII: S0142-9612(25)00620-9

DOI: https://doi.org/10.1016/j.biomaterials.2025.123701

Reference: JBMT 123701

To appear in: *Biomaterials*

Received Date: 17 April 2025

Revised Date: 26 August 2025

Accepted Date: 12 September 2025

Please cite this article as: Zhao S, Wu L, Taiyari S, Li H, Sun J, Chen J, Song W, Cerletti M, A digitally programmable 3D microenvironment directs satellite cell function, *Biomaterials*, https://doi.org/10.1016/j.biomaterials.2025.123701.

A digitally programmable 3D microenvironment directs satellite cell function

Shudong Zhao[1,2,3], Lei Wu[4,5], Sara Taiyari[1,2,3], Huiliang Li[6], Jianfei Sun[4], Jishizhan Chen[1,2,3], Wenhui Song[4*], Massimiliano Cerletti[1,2,3*]

[1]Tissue Repair and Regeneration Centre, Division of Surgery & Interventional Science, University College London, Royal Free Campus, London NW3 2PF, UK

[2]Centre for Surgical Innovation, Organ Repair and Transplantation (CSIORT), University College London, Royal Free Campus, London NW3 2PF, UK

[3]Centre for Bioengineering and Surgical Technology (BEST), University College London, Brockley Hill, Stanmore HA7 4AP, UK

[4]Centre for Biomaterials in Surgical Reconstruction and Regeneration, University College London, Royal Free Campus, London NW3 2PF, UK

[5]Department of Engineering Mathematics and Bristol Robotics Laboratory, University of Bristol, Bristol BS8 1TW, UK

[6]Wolfson Institute for Biomedical Research, Division of Medicine, Faculty of Medical Sciences, University College London, London WC1E 6BT, UK

*Corresponding authors. Email: w.song@ucl.ac.uk (W.S.); m.cerletti@ucl.ac.uk (M.C.)

Abstract

Skeletal muscle stem cells, also known as satellite cells, have remarkable self-renewal abilities in response to muscle injury, playing a vital role in muscle regeneration and repair. However, disruptions in the satellite cell niche caused by severe trauma or surgery can hinder natural regeneration. Additionally, challenges such as limited availability of human donors and primary cells, difficulties in scaling satellite cell expansion, and storage issues present significant barriers. Therefore, developing engineered platforms that create optimized micro-niche environments to support muscle stem cells and promote muscle cell activity is crucial. Using non-direct 3D printing-guided phase separation technology and skeletal muscle extracellular matrix (ECM) hydrogel, we developed a digitally programmable, user-friendly, customizable, and biofunctional 3D platform that mimics the hierarchical porous structure and microenvironment of natural ECM. Notably, the synergistic combination of natural and synthetic matrices improves scalable satellite cell growth, supports autonomous myotube contraction, and accelerates *in vivo* myofiber and blood vessel formation, paving the way for increased production of myogenic precursors, cell therapies, and treatments for traumatic muscle injuries.

Keywords

Satellite cells, skeletal muscle regeneration, digitally programmable porous platform, non-direct 3D printing, decellularization, and extracellular matrix (ECM)

INTRODUCTION

Skeletal muscle repair relies on a dynamic interaction between satellite cells and their microenvironment, enabling effective regeneration after injury [1, 2]. As precursors to skeletal muscle, activated satellite cells help maintain the stem cell pool and differentiate into fusion-competent myoblasts that fuse with existing myofibers and with each other to repair the muscle. Satellite cells reside in a membrane-enclosed niche between the plasma membrane and the basal lamina surrounding the myofibers, adhering to collagen type IV and laminin through integrins that connect to the extracellular matrix (ECM) protein nidogen. As a key component of the basal lamina, the ECM provides biomechanical support and biochemical signals to satellite cells, influencing their activity, cellular responses, and muscle morphogenesis following injury [1-3]. Satellite cells play a vital role in postnatal muscle growth, hypertrophy, and regeneration. They are the primary resource for developing transplantation strategies for neuromuscular disorders and muscle loss. However, challenges exist in sourcing, isolating, expanding, and storing these primary cells, which require strict quality control to ensure reliable data from donors of various ages and conditions. Additionally, muscle stem cells gradually lose their self-renewal ability when removed from their *in vivo* niche, leading to myoblast differentiation and reduced graft potential [4].

Furthermore, the limited availability of human donors makes it challenging to increase satellite cell production and maintain a consistent cell population for therapeutic applications. In cases of severe muscle injury, the absence of a satellite cell niche impairs the muscle's ability to repair itself, leading to structural, functional, and aesthetic deficits that often necessitate surgery [5, 6]. Effectively restoring significant muscle loss usually involves functional muscle transfer. While autologous skeletal muscle flaps are commonly used and considered the standard treatment, they have notable disadvantages, such as donor site morbidity and limited tissue availability [6].

Non-direct 3D printing technology shows promise for creating cellular micro-niche environments. Specifically, synthetic polymers designed for muscle cell growth provide mechanical support, customizable shapes for irregular wounds, and internal structures that mimic the ECM's porous architecture [7]. Recently, there has been a growing interest in using decellularized tissues and organs as implants for tissue reconstruction [8-10]. Decellularized muscles have demonstrated potential in attracting host cells to promote *in vivo* muscle regeneration in animal models [10-13]. However, these biomaterials often face challenges in supporting long-term myofiber regeneration in cases of significant volumetric muscle loss, as they provide limited mechanical support and can be challenging to tailor for patient-specific wound sites with complex shapes and sizes [13, 14]. ECM components, including collagen [15], fibronectin [16], and hyaluronic acid [17], are often used to develop substrates that display high biocompatibility and functional groups. These traits enhance the effective conjugation of growth factors and support tissue regeneration; however, challenges such as the limited number of functional groups compared to native ECM, high costs, inadequate mechanical properties, and limitations in manufacturing methods (e.g., crosslinking or freeze-drying) impede the large-scale production of biomaterials with complex shapes and interconnected porous structures. Consequently, this often leads to slow cell infiltration and vascular ingrowth, impairing the complete integration of the construct.

Additionally, natural components, whether hydrogels or crosslinked foams, are susceptible to enzymatic degradation. This reduction in their mechanical properties renders them unsuitable for providing the durable, long-term support needed for proper tissue growth. Unlike natural products, synthetic polymer-based biomaterials have more precisely controlled physical and chemical properties, including higher mechanical strength. These biomaterials are versatile and can be customized to meet specific needs through molecular design and various processing techniques, such as 3D printing, which enables better control over complex internal structures like pore size and porosity. Polycaprolactone (PCL), a biodegradable polyester, is widely used in medical applications due to its high biocompatibility, purity, tunable mechanical properties, and costeffectiveness in material development [18, 19]. PCL-based constructs developed to date are mainly produced using direct 3D printing methods, such as fused deposition modeling (FDM) and micro-extrusion. They exhibit high stiffness, with an elastic modulus ranging from 30 to 150 MPa. These constructs are particularly suitable for hard tissue applications, such as osteochondral and bone tissue repair, but are not ideal for soft tissues, like skeletal muscle [20-22].

In this study, we developed a unique, digitally controlled, hierarchically porous 3D biofunctional platform (d3D-BP) optimized for growing muscle satellite cells, using a skeletal muscle extracellular matrix hydrogel (dECM) and a non-direct 3D printing-guided phase separation (3D-PPS) technique. The d3D-BP features a programmable and adjustable internal structure and surface topography, along with mechanical and biological properties that closely mimic the skeletal muscle environment. These innovations create a 3D micro-niche with satellite cell recognition sites, significantly enhancing the *in vitro* maintenance of muscle stem cells, supporting autonomous myotube contraction, and promoting *in vivo* skeletal muscle regeneration and vascularization.

RESULTS

Digitally programmable, hierarchical porous structures with adjustable properties within a 3D bio-assembled system

Satellite cells respond to the mechanical, chemical, and biological features of their microenvironment. Due to the complex cell culture conditions and microenvironment, developing scalable and effective methods for maintaining and proliferating satellite cells *in vitro* remains a significant challenge [23-25].

Our study introduces the 3D-PPS method, which combines 3D printing, resin infusion molding, and phase separation technology to develop a 3D platform with a hierarchical, porous, and compliant structure that simulates the properties of skeletal muscle ECM. We fabricated 3D-BP by injecting a PCL/dimethylformamide (DMF) solution into an aqueous-soluble polyvinyl alcohol (PVA) negative mold with pre-designed interconnected microchannels, serving as a sacrificial template created using an FDM 3D printer. This was followed by PCL coagulation and PVA dissolution in deionized water, resulting in surfaces with increased porosity (**Fig. 1A**). These porous surfaces were analyzed using scanning electron microscopy (SEM) (**Fig. 1B-C**). Different weight ratios of PCL/DMF solutions (10%, 15%, and 20% w/v) produced 3D-BPs, named 3D-BP-10%, 3D-BP-15%, and 3D-BP-20%. Unlike traditional phase separation at the macro-scale interface, this separation is driven by diffusion and exchange of DMF and diH_2O within interconnected microchannels that have larger surface areas and slower diffusion rates. Consequently, porous structures form on a smaller scale, from micro to nano, compared to the smooth, solid surface of a fully PCL 3D direct-printed sample (3D-DP) (**Fig. 1D-F**). Chart 1E displays a broad range of pore size distributions, from 400 μm to 10 nm, with variations influenced by the PCL concentration, as determined through mercury intrusion porosimetry [26]. In 3D-BP-10%, formed from a low PCL concentration, digitally defined macropores (100-1000 μm) coexist with micropores, which constitute the dominant inner structure (~50%, <10 μm), while also featuring a significant number of nanopores (11.39%, <100 nm). Further analysis revealed that 3D-BP-10% achieved the highest porosity (>95.77%) and specific surface area (>52.67 m^2/g) (**Fig. 1E-F and Table S1-2**). As expected, 3D-DP mainly showed macropores (>95.44% of pores, size >10 μm), with minimal presence of micropores (<5% of pores, size <10 μm), resulting in low porosity (49.43%) and specific surface area (0.78 m^2/g) (**Fig. 1E-F and Table S1-2**). The results also indicated that the 10% PCL 3D-BP had the lowest density (0.048 g/cm^3) compared to the densities of 15% PCL (0.068 g/cm^3), 20% PCL (0.089 g/cm^3), and 100% PCL (0.58 g/cm^3) (**Table S1**).

3D-BPs significantly increased surface roughness, with peaks and valleys serving as physical anchors for cell spreading. This promotes the formation of strong focal adhesions that connect to the internal cytoskeleton, regulate cellular signaling pathways, and influence cell behavior. High wettability enhances protein absorption and further supports cell adhesion. (**Fig. 1G-I**). Additionally, the tensile elastic modulus (<3.53 MPa) and compressive modulus (<847 kPa) of 3D-BPs decreased significantly—by more than 10 and 40 times, respectively—compared to those of 3D-DP (46.28 MPa and 40.30 MPa). This reduction also applies to the tensile yield strength (decreasing from 0.32 to 0.12 MPa, a 62% decrease) and tensile toughness (increasing by over 50%) (**Fig. 2A-D and Table S1**). Therefore, the soft, ductile mechanical properties, high porosity, and increased surface area make 3D-BPs suitable for soft tissue repair and regeneration. The 10% PCL 3D-BP, with the highest compliance and ductility, stands out as the best option for supporting muscle tissue growth, showing a tensile modulus of 914 kPa and a compressive modulus of about 303 kPa, where the modulus of a fiber bundle ranges from 58.83 to 462.5 kPa (**Fig. 2A-D and Table S1**) [27].

Compared to current PCL-based scaffolds for muscle regeneration, the 3D-BPs exhibit high compliance at ultra-low density (high porosity), even rivaling decellularized muscle and hyperelastic polyurethane elastomer foams, while also displaying more defined porous structures (**Fig. 2F and Table S4**) [28-36]. This makes them ideal for applications requiring flexibility and strength, such as tissue reconstruction and regenerative medicine. Notably, the superior mechanical properties of the 3D-BPs stem from their unique semi-crystalline structure, characterized by a low degree of crystallinity in the porous PCL structures formed during the 3D-PPS process. The crystallinity of the 3D-BPs, estimated from the endothermic peak and measured by differential scanning calorimetry (DSC), decreases with lower PCL concentrations (29.74%, 27.09%, and 24.29% for 20%, 15%, and 10% 3D-BP, respectively), and is lower than that of the 3D-DP (33.83%) (**Fig. 2E and Table S3**). Interestingly, the endothermic peak becomes sharper, and the peak temperature slightly increases as the PCL concentration decreases, indicating a more uniform crystalline structure in the 10% PCL 3D-BP dilute solution. Therefore, the overall hierarchical structure, improved surface, and mechanical properties of 3D-BP-10% create an optimized platform suitable for both *in vitro* and *in vivo* studies.

The cytocompatibility of the 3D bio-assembled system

In addition to their tunable mechanical properties, 3D-BPs demonstrated optimal compatibility with myogenic cells, as shown by metabolic activity and proliferation tests using C2C12 cells (**Fig. S1**). By day 1 post-seeding, we observed increased C2C12 cell proliferation in all three 3D-BPs compared to the 3D-DP, indicating rapid cell attachment. By day 4 post-seeding, C2C12 cell numbers consistently increased in all 3D-BPs, with the 10% 3D-BP showing the highest cell growth at each time point (**Fig. S1A-D**). Through immunostaining assays, we examined cell morphology, cell density, and the smallest gap area within the cells (**Fig. S1A-B**). Compared to 3D-DP controls, cell-seeded 3D-BPs also showed improved metabolic activity, as indicated by the AlarmBlue™ assay and the total DNA assay (**Fig. S1C-D**). This suggests that porous, rough surfaces promote the viability and proliferation of myogenic cells, aligning with findings for other cell types, such as rat bone marrow mesenchymal stem cells [37], human mesenchymal stem cells [38], and fibroblasts [39]. Consequently, the rapid proliferation of C2C12 cells led to differentiation and myotube formation, first observed in the 10% 3D-BP (data not shown). These results indicate that the 10% 3D-BP fosters a conducive 3D microenvironment for myogenic cell growth and differentiation, which holds promise for future developmental stages and translational applications.

Characterizing the decellularized muscle extracellular matrix hydrogel (dECM)

Previous studies suggest that decellularizing and implanting skeletal muscle can enhance muscle regeneration [10, 11]. In this study, we decellularized limb skeletal muscles to remove cell nuclei and processed them to produce an ECM-protein-enriched hydrogel as a functionalization factor for the 3D-BP (**Fig. S2A-D**). The protein composition of dECM was analyzed using liquid chromatography-mass spectrometry (LC-MS), identifying 1,991 peptides. Using the MatrisomeDB database [40], we annotated a total of 127 dECM proteins (referred to as "Matrisome") into six groups: three core matrisome categories (18.11% collagens, 37.80% glycoproteins, and 11.81% proteoglycans) and three matrisome-associated protein categories (18.90% regulators, 10.24% affiliated proteins, and 3.15% secreted proteins) (**Fig. 3A-B and Table S5**). These categories include collagen V and collagen VI, known as key components of the satellite cell niche and essential for maintaining cell quiescence and regulating muscle regeneration [41, 42]; laminin, a glycoprotein of the ECM that binds to the α7/β1 integrin on the satellite cell membrane and regulates self-renewal and migration [43-45]; and fibronectin, also a glycoprotein of the cell niche, whose loss has been reported to compromise the regenerative capacity of skeletal muscle [46]. This list also includes ECM proteoglycans involved in muscle regeneration, such as biglycan [47], decorin [48], fibromodulin [49], and lumican [50], as well as matrisome-associated proteins that participate in satellite cell activation and tissue regeneration, including plasminogen [51] and members of the annexin family [52-54]. In addition to these proteins, dECM may contain other unidentified proteins that directly or indirectly regulate the behaviors and functions of satellite cells. However, their exact roles remain unclear and warrant future investigation (**Table S5**).

Enhanced satellite cell function in 2D dECM substrates and 3D bio-assembled systems

Satellite cells are a crucial source of stem cells for maintaining skeletal muscle, and their quantity and function significantly impact the efficiency of muscle repair. To examine how dECM affects satellite cell function, freshly isolated satellite cells were seeded onto dECM hydrogel or collagen/laminin-coated plates (control). The ratio of Pax-7 to myogenin expression, along with the BrdU signal, was used to assess the rates of proliferation and differentiation. In satellite cell cultures, Pax-7, a key marker of satellite cells, gradually decreases, while differentiation markers, such as myogenin, increase in expression [55]. Notably, dECM hydrogel-coated plates showed more than twice the number of cells compared to no-dECM controls by day 5. This indicates that dECM hydrogel is an ideal substrate for promoting satellite cell proliferation (**Fig. 3C-D**). This finding was further confirmed by a significant rise in Pax-7$^+$/BrdU$^+$ satellite cells in dECM hydrogel-coated plates (59.45%) compared to no-dECM controls (44.72%) (**Fig. 3E-F**).

In addition to monitoring satellite cell expansion, we evaluated cell differentiation under expansion culture conditions by examining Pax-7$^-$myogenin$^+$ myoblasts. Interestingly, although over 99% of cells were Pax-7$^+$ in both dECM and no-dECM control conditions, Pax-7$^+$/myogenin$^-$ satellite cells were significantly more prevalent in dECM hydrogel samples (67.57% vs. 35.22%). Conversely, Pax-7$^+$/myogenin$^+$ transitory cells were considerably less frequent (31.90% vs. 63.95%) in dECM hydrogel samples compared to no-dECM controls, emphasizing the critical role of dECM in guiding satellite cell activity (**Fig. 3G-H**). Pax-7$^-$/myogenin$^+$ cells were rarely observed, and no significant difference was found between the two groups (**Fig. 3H**).

Interestingly, the effect of dECM hydrogel was amplified in 3D cultures. The expansion of satellite cells seeded in dECM-functionalized 3D-BP (d3D-BP) was three times greater than in the non-dECM-functionalized platforms used as controls (**Fig. 4B**). This was supported by a significantly higher number of Pax-7$^+$ satellite cells stained with BrdU in d3D-BP compared to the 3D-BP controls (63.96% vs. 43.7%) (**Fig. 4C**). A substantial increase in Pax-7$^+$/myogenin$^-$ satellite cells (96.17%) was observed in d3D-BP, alongside a decrease in Pax-7$^+$/myogenin$^+$ transient cells (3.08%), while Pax-7$^-$/myogenin$^+$ cells remained significantly low in both cultures (**Fig. 4D**). Notably, d3D-BP exhibited approximately a threefold increase in Pax-7$^+$/myogenin$^-$ satellite cells compared to 2D cultures. This suggests that d3D-BP provides a superior micro-niche for satellite cell maintenance, thereby delaying myogenic differentiation.

The formation of multinucleated myotubes in d3D-BP under differentiation conditions showed higher myogenic compatibility compared to the 3D-BP control (**Fig. 4E**). This was confirmed by confocal microscopy multilayer screening, which revealed MyHC$^+$ elongated myotubes across different layers (**Movie S1**). Twitching myotubes were captured on the strut surface and extended toward the digitally programmed macropores of the d3D-BP, rather than lying on top of the material, which appears dark under light microscopy and makes them difficult to visualize. Myotubes occupied over 20% of the initial pore space during a 14-day culture period. Remarkable autonomous contractions were observed spontaneously at a frequency of 1-2 Hz, with varying local contraction velocities (**Fig. 4F-H, and Movies S2-4**). Analysis of contractions in three representative myotube areas, designated as Area 1, Area 2, and Area 3, reveals that peak contractions occurred at different time points within 10 seconds (0.67 s, 3.33 s, and 9.67 s, respectively) (**Fig. 4F a-c and Movies S2-4**). Displacement vectors (marked in green) indicate visible myotube contraction, mainly detected near the edges of the d3D-BP (**Fig. 4F a-c**). The magnitudes of peak contraction velocities across Areas 1 to 3 are illustrated in heat maps, with the maximum transient contraction velocity reaching approximately 60 μm/s in Area 1 (yellow arrows, **Fig. 4F d-f**). The mean contraction velocity spectra of each myotube cluster over 10 seconds (**Fig. 4G**) display distinctly different dynamic profiles for each local contraction, without revealing a clear trend. These mean peak contraction velocities ranged from 2.79 μm/s to 27.23 μm/s, as summarized in Fig. 4H, with an average peak contraction velocity of 11.62 μm/s. Unlike traditional 2D skeletal muscle satellite cell cultures, the more complex local environment provided by d3D-BP influences *in vitro* skeletal muscle formation with various myotube contraction functions.

Biofunctionalized 3D-BP implants enhance satellite cell activity and support skeletal muscle regeneration

Satellite cells are a vital source of stem cells necessary for maintaining and regenerating skeletal muscle, as their quantity and function significantly influence the success of muscle repair. Given the robust myogenic activity *in vitro* and the versatility of d3D-BP, we hypothesized that d3D-BP could also serve as a scaffold for skeletal muscle repair in implantation strategies. To test this, d3D-BPs and 3D-BP controls were implanted into the tibialis anterior (TA) muscles of C57BL/6 mice. After four weeks, the TA muscles were harvested, processed, and analyzed to measure centrally nucleated, newly formed myofibers (**Fig. 5A**). This analysis revealed an increase in the size of these myofibers and a higher proportion of large myofibers in TAs implanted with d3D-BP, indicating faster regeneration (**Fig. 5B-D**). Notably, the newly formed myofibers in the d3D-BP group were nearly twice as large (498.74 μm²) compared to the 3D-BP controls (246.30 μm²) (**Fig. 5C**). Myofiber size distribution analysis showed that most regenerative myofibers in the 3D-BP control group measured less than 300 μm² (71.52%, grey bars); this percentage decreased by nearly threefold in the d3D-BP group, with only 25.20% of myofibers measuring below 300 μm². As expected, most regenerative myofibers in d3D-BPs ranged from 300 to 600 μm² (59.81%, yellow bars) (**Fig. 5D**). Interestingly, myofibers larger than 900 μm² comprised over 10% of the total regenerative myofibers in d3D-BPs, indicating a substantial increase compared to the 3D-BP controls (1.15%) (**Fig. 5D**). Unlike the 3D-BP control groups, several large mature myofibers with peripheral nuclei were observed in the d3D-BPs (**Fig. 5B**). We also evaluated myofiber function by measuring ATPase levels. Assessing ATPase content in muscle fibers involves determining the amount of ATP available for muscle contraction. This is essential for understanding muscle performance, energy metabolism, and fatigue (**Fig. S3A and B**). In summary, we found significantly larger newly formed myofibers (over 400 μm²), a higher percentage of mature myofibers, and fewer slow-twitch Type I fibers in d3D-BPs, indicating a rapid repair process.

Additionally, sporadic inflammatory infiltration was observed among myofibers, mainly in the 3D-BP control group, indicated by the presence of CD8$^+$ and CD11$^+$ cells, suggesting delayed regeneration (**Fig. S3C-F**). Along with the robust regenerative activity of d3D-BPs, we measured the percentage of CD31$^+$ blood vessels and vessels containing erythrocytes, which are crucial for oxygen transport during skeletal muscle repair and regeneration. CD31$^+$ blood vessels increased threefold in d3D-BPs compared to 3D-BP controls, supported by vessels with a higher density of red blood cells (**Fig. 5E-F and Fig. S3G-H**). Similarly, as seen in healthy skeletal muscle, newly formed blood vessels displayed an aligned axial pattern along the muscle fibers (yellow arrows), demonstrating the *in vivo* biocompatibility and angiogenic potential of the composite d3D-BP.

DISCUSSION

The properties of biomaterials—composition, structure, and signaling—guide cells and tissues to enhance regenerative capabilities, which are essential for effective implantation strategies and trauma treatments [56-60]. Electrospinning is a well-documented method for producing porous PCL-based constructs. Studies have shown that, due to protein adsorption and cell attachment, electrospun PCL-based porous nanofibers promote *in vitro* myoblast attachment and differentiation [30, 61-64]. However, the microporous nature of this construct limits cell infiltration throughout its structure, and the limited z-axis resolution poses challenges in creating large, thick constructs [65]. Compared to d3D-BP, this membrane-like structure provides a less complex 3D environment for cell growth, featuring a similar yet non-tunable microporous surface and macro-caliber interconnecting channels within the construct. This underscores the crucial importance of porosity and interconnectivity for nutrient diffusion and cell infiltration in potential implants [56]. Alternative methods, such as thermal drawing and salt leaching, produce 3D porous structures for volumetric muscle loss (VML) by layering hollow PCL microfibers into large constructs [35, 66]. However, this technique faces significant challenges in achieving robust fiber bonding, which is crucial for providing long-term mechanical support in load-bearing applications. The lack of interconnected channels between fibers also restricts cell migration and communication, adversely impacting muscle regeneration.

Unlike other methods, the 3D-PPS technology creates digitally controlled, hierarchically porous structures that ensure optimal compliance and strength, making them ideal for long-term support in myo-trauma treatments. The extensive interconnected channels of 3D-BP facilitate efficient nutrient exchange, cell infiltration, and communication, while microporous features enhance protein absorption and cell attachment, thereby improving tissue integration and regeneration. Additionally, the effectiveness of the muscle dECM hydrogel was demonstrated by the improved function of muscle stem cells in both two-dimensional and three-dimensional environments, as shown by a significantly higher percentage of Pax-7$^+$/myogenin$^-$ satellite cells compared to those without dECM hydrogel (2D: 67.57% vs. 35.22%; 3D: 96.17% vs. 75.22%). d3D-BP cultures yield nearly three times the percentage of satellite cells compared to 2D cultures (96.17% vs. 35.22%). It is reasonable to hypothesize that the inductive effect arises from synergistic interactions between satellite cells and micro-niche proteins, as dECM includes a mixture of muscle ECM proteins such as various collagens, proteoglycans, and glycoproteins (including laminin and fibronectin), which are known to regulate satellite cell function [41-45, 67, 68].

Meanwhile, other dECM proteins, whose exact roles remain uncertain, may individually and synergistically influence satellite cell behavior and muscle regeneration, both directly and indirectly. This data highlights d3D-BP’s ability to replicate the satellite cell micro-niche environment, underscoring its essential functions. Another influential factor may be the stiffness of the substrate, as satellite cells have been shown to proliferate more readily on softer surfaces, with substrate stiffness affecting their proliferation behavior [69-72]. Notably, on 2D polystyrene culture plates, stiffness is measured at 3 GPa, which is over 9,000 times harder than d3D-BP at 0.303 MPa. All these characteristics of d3D-BP—including lower stiffness, increased total specific surface area, porosity, a higher volume of absorbed dECM proteins per unit mass, adhesion between substrates and cells, and multidimensional stimulation—significantly contribute to maintaining satellite cells.

Additionally, seeded d3D-BP under myogenic cell differentiation conditions shows the ability to direct the development of mature myotubes derived from satellite cells that can contract spontaneously—an achievement not yet reported in other studies. Most engineered contracting myotubes typically originate from myogenic C2C12 cell lines or myoblasts derived from genetically modified induced pluripotent stem cells (iPSCs), often requiring additional stimuli, such as electrical or optogenetic stimulation, to cause contraction [73-76]. This synergistic interaction between mature myotubes and a supportive 3D microenvironment that mimics the natural features of skeletal muscle could provide an *in vitro* platform for disease modeling and drug testing.

Ultimately, enriching the 3D-BP with muscle ECM proteins has proven more effective for muscle regeneration *in vivo* than commonly used decellularized tissues, such as dermis, small intestine, and urinary bladder, for muscle repair [10, 11, 77]. The d3D-BP implanted in TA muscles significantly enhanced the formation of newly developed myofibers, with an average cross-sectional area ranging from 300 to 500 μm^2. This level of myofiber regeneration exceeded previous reports, demonstrating improved skeletal muscle repair and *in situ* angiogenesis [35]. Given the potential of 3D-PPS technology to modify both outer and inner structures, we anticipate developing a 3D-BP with anisotropic large-caliber channels and high interconnectivity that can replicate myofiber alignment and potentially treat traumatic muscle injuries, thereby fulfilling an unmet clinical need.

MATERIALS AND METHODS

3D-BP design and manufacturing

A sacrificial PVA (eSUN) mold with a pre-designed internal porous structure was created using a MakerBot Replicator (5th Generation, USA) 3D printer. The PVA mold was filled with a PCL (Mn = 80,000)-dimethylformamide (DMF) solution and then immersed in deionized water (diH_2O) to facilitate PCL coagulation and PVA dissolution. 3D-BPs were produced with different PCL concentrations (10%, 15%, and 20% PCL/DMF ratio, w/v%). The control consisted of a fused deposition modeling (FDM) 3D-printed PCL (100% PCL). All chemicals were sourced from Sigma-Aldrich (Sigma-Aldrich Limited, MO, USA) unless otherwise specified.

3D-BP physical and mechanical characterization

The morphology and structure of the 3D-BP were examined using a scanning electron microscope (SEM) (Carl Zeiss EVOLS HD 15, Germany). Surface roughness was measured with Olympus LEXT software on a series of laser confocal images capturing the entire surface of the platform (Olympus OLS4100, UK). Porosity (ρ) was calculated using the formulas: $\rho = (1 - \rho_a/\rho_b) \times 100\%$ and $\rho_a = \omega/(\pi r^2 h)$. The bulk density of PCL (ρ_b) was 1.145 g/cm^3, while the apparent density (ρ_a) was determined based on the average weight (w), radius (r), and height (h) of six pre-cut sample disks. A mercury intrusion porosimeter (Quantachrome Poremaster 60GT, Quantachrome, UK) was used to evaluate pore size and distribution. Mechanical properties were assessed by measuring static tensile strength (Instron 5655 tester, Instron Ltd., USA) and compressive strength (EZ-LX test machine, Shimadzu, Japan) at room temperature. Six tensile specimens (10 mm × 40 mm × 1.2 mm) and six compressive cubes (10 mm × 10 mm × 10 mm) were tested. Surface wettability was evaluated by measuring the static contact angle with the captive bubble method using a KRÜSS DSA 100 system (KRÜSS, Hamburg, Germany). One bubble per sample (diameter = 15.6 mm, height = 1.2 mm) and six samples per platform were measured at room temperature. The thermal properties were analyzed using a Differential Scanning Calorimeter (DSC, PerkinElmer, USA) with a heating scan from -72 $^\circ$C to 150 $^\circ$C at a rate of 10 $^\circ$C/min. Crystallinity was determined based on the melting enthalpy of 100% crystalline PCL (135 J/g).

Protein absorption assay

Protein absorption was assessed by measuring the residual bovine serum albumin (BSA) remaining after absorption (Pierce™ BCA Protein Assay Kit, Thermo Fisher Scientific, MA, USA). Each platform type (diameter = 15.6 mm; height = 1.2 mm, n = 6 replicates) was immersed in 1 ml of BSA solution (250 µg/ml) at 37 °C for 0.5 h, 1 h, 2 h, and 4 h. After each incubation period, the absorbance of the remaining BSA in the solution was measured at 562 nm using a Fluoroskan Ascent FL microplate fluorometer and luminometer (Thermo Labsystems, USA). The volume of residual BSA in the solution and the amount absorbed by the scaffold were then calculated.

3D-BP cytocompatibility assay

C2C12 myogenic cells (ATCC® CRL-1772™) were seeded onto a sterilized 3D-BP at a density of 200,000 cells (diameter = 15.6 mm, height = 1.2 mm, n = 6 replicates) in a culture medium containing 10% Fetal Bovine Serum (FBS) and 1% Penicillin/Streptomycin (P/S) in Dulbecco's Modified Eagle Medium (DMEM) from Thermo Fisher Scientific, with the media changed every other day. Cell viability and proliferation were evaluated using the alamarBlue™ assay and a total DNA kit (Thermo Fisher Scientific) on days 1, 4, 7, and 14. Cells were stained with F-actin (green, Thermo Fisher Scientific) and Hoechst (blue, Thermo Fisher Scientific).

Extracellular matrix hydrogel derived from decellularized muscle (dECM)

Limb skeletal muscles were harvested from 3- to 4-month-old C57BL/6 mice (Charles River Laboratories, UK), transferred to ultrapure water (1 g/30 mL), and agitated for two days with three daily water changes. They were then treated with 1% (w/v) sodium dodecyl sulfate (SDS) for two days, with one change each day, followed by a 30-minute treatment with 1% (v/v) Triton X-100. The muscles were washed with ultrapure water for an additional two days, agitated, and the water was changed daily. Finally, the decellularized skeletal muscles were frozen and lyophilized using a benchtop freeze dryer (Labconco Corporation, MO, USA), then crushed. The processed muscles were dissolved at 0.1% (w/v) in a pepsin/acetic acid solution (0.5 M) for three days with continuous agitation. After digestion, the solution was left to settle and then filtered. The dECM hydrogel was formed through natural water evaporation, which prevents altering the dECM protein structures caused by crosslinking, potentially affecting protein function. The rheological behavior of dehydrated dECM gel and dECM coating solution was assessed using a rheometer (NETZSCH Kinexus) equipped with a parallel-plate geometry. All measurements were performed at 37 °C with a 0.3 mm gap. Strain sweeps (0.1–100% strain, 1 Hz) were conducted to identify the linear viscoelastic region, followed by frequency sweeps (0.1–10 Hz) at a constant strain of 0.1%. Storage modulus (G′), loss modulus (G″), and complex viscosity (η^*) were recorded for comparison.

Mass spectrometry and data analysis

Peptides from dECM were analyzed using liquid chromatography-mass spectrometry (LC-MS, Q Exactive mass spectrometer, Thermo Fisher Scientific, USA). Proteins were identified using MaxQuant software and classified with the MatrisomeDB 2.0 database [40].

Satellite cell isolation

Single myofibers and myofiber-associated cells were isolated from intact limb muscles, including the extensor digitorum longus, gastrocnemius, quadriceps, soleus, tibialis anterior, and triceps brachii. After isolation, myofiber-associated cells were stained for FACS to identify muscle stem cells characterized by CD45$^-$Sca-1$^-$Mac-1$^-$CXCR4$^+$β1-integrin$^+$ [78-80]. FACS data were collected using the FACSAria Fusion machine (Becton Dickinson (BD), Franklin Lakes, NJ, USA).

Immunofluorescence staining

Satellite cells, myoblasts, and myotubes were fixed in 4% PFA for 20 minutes (PFA, Thermo Fisher Scientific, USA), followed by permeabilization with 0.1% Triton X-100 for 30 minutes. They were then blocked with 5% normal goat serum for 30 minutes (Thermo Fisher Scientific) before incubation with primary and secondary antibodies. The antibodies used included: Alexa Fluor™

488 Phalloidin (1:300, three hours, room temperature, Thermo Fisher Scientific); MF-20 (1:200, three hours, room temperature, Developmental Studies Hybridoma Bank (DSHB, USA)); Pax-7 (1:100, overnight, 4 °C, DSHB); Myogenin (M-225) (1:200, three hours, room temperature, Santa Cruz Biotechnology, USA); Goat Anti-Mouse IgG Alexa Fluor 594 (1:400, 1.5 hours, room temperature, Thermo Fisher Scientific); Goat Anti-Mouse IgG Alexa Fluor 488 (1:400, 1.5 hours, room temperature, Thermo Fisher Scientific); Goat Anti-Rabbit IgG Alexa Fluor 594 (1:400, 1.5 hours, room temperature, Thermo Fisher Scientific). After each incubation, the cells were washed three times with PBS for five minutes each. The nuclei were labeled with Hoechst 33342 or DAPI (Thermo Fisher Scientific).

BrdU incorporation and detection

Satellite cells were cultured overnight in BrdU medium (20% horse serum, 1% P/S, and 10 nM 5-Bromo-2’-deoxyuridine (5-BrdU) in F-10 medium), fixed with PFA (4% for 20 minutes), permeabilized with Triton X-100 (0.1% for 30 minutes), treated with DNA denaturation solutions (1N HCl for 10 minutes on ice; 2N HCl for 10 minutes; phosphate/citric acid buffer, pH 7.4, for 10 minutes), blocked with normal goat serum (5% for 30 minutes), and incubated with BrdU antibody (1:200, overnight at 4 °C, MoBU-1, Alexa Fluor 594, Thermo Fisher Scientific). Immunofluorescence images were captured using a Leica DMI4000 B inverted microscope (Leica). Ten fields per sample and three replicates per group were analyzed for BrdU$^+$ cells.

Satellite cell cultures in two-dimensional and three-dimensional settings

Plates and 3D structures were treated with a standard coating solution (0.01% v/v collagen and 0.1% v/v laminin from Thermo Fisher Scientific) or dECM coating for 20 minutes, followed by air drying. Muscle satellite cells were seeded in 24-well plates at a density of 50,000 cells per well or 100,000 cells in d3D-BP-10% in F-10 medium (Ham’s F-10 Nutrient Mix, containing 20% horse serum and 1% penicillin/streptomycin from Thermo Fisher Scientific). Fibroblast growth factor (bFGF, Sigma) was added daily at five ng/ml, with 50% of the medium replaced every other day. Pax-7, myogenin, and BrdU signals were assessed to evaluate the expansion of muscle satellite cells. Myogenic differentiation and myotube formation were induced by switching the growth medium to a differentiation medium containing 5% horse serum. After 14 days of induction, the contractile activity of the newly formed myotubes was recorded using an Olympus microscope with a high-resolution video camera at a frame rate of 12 frames per second. Data were analyzed with PIVlab in MATLAB, which tracked the local displacement of small interrogation regions between consecutive frames to accurately quantify contraction velocity in micrometers per second (μm/s) for spontaneous myotube contractions. Myotubes were fixed in 4% paraformaldehyde (PFA) from Thermo Fisher Scientific and stained with MyHC. MyHC$^+$ elongated myotubes across various d3D-BP layers were visualized using Leica SP8 DM6 confocal microscopy multilayer screening (Movie S1).

Intramuscular implantation of d3D-BP

C57BL/6 mice (3 months old, Charles River Laboratories, UK) were shaved preoperatively and anesthetized with 4% isoflurane for induction, followed by 2% isoflurane for maintenance, along with a mixture of O_2 and N_2O. Skin incisions and muscle pockets were made along the tibialis anterior (TA) muscles, and d3D-BPs and 3D-BP controls (2 mm x 1.2 mm x 1.2 mm, n = 6 per group) were inserted and fixed within the muscle pockets. Four weeks after implantation, the C57BL/6 mice were euthanized by CO_2 asphyxiation, and TA muscles were harvested for analysis. All procedures received approval from the Institutional Animal Care and Use Committees at UCL.

Histology and immunostaining

Harvested implanted TAs were frozen in pre-cooled 2-methylbutane before being sectioned into 8-10 µm-thick slices using a Cryotome™ FSE Cryostat. Hematoxylin and Eosin (H&E) staining was performed with the H&E Stain Kit (Vector Laboratories). Images of the implanted area were captured using the Olympus DP80 microscope, and approximately 400 centrally nucleated regenerating myofibers were counted per field with ImageJ software (NIH, USA). ATPase staining involved pre-incubation with pH 4.5 buffer for 2 minutes at 22–24°C, followed by a quick rinse with water. The sections were then incubated in ATP buffer at room temperature for 20–25 minutes, rinsed 2–3 times with a 1% $CaCl_2$ solution, stained with 1% Azure A for 1 minute, and then rinsed. Preparations were dehydrated in 50%, 70%, 95% and 100% ethanol, cleared with xylene, and mounted with DPX (Sigma). Serial muscle sections were treated with 0.1% Triton X-100 for 30 minutes, blocked with M.O.M. blocking reagent for another 30 minutes (Vector Laboratories), and incubated with CD31 (1:300, MERCK) for 2 hours at room temperature, followed by incubation with FITC-conjugated anti-Armenian hamster IgG (1:200) for 1 hour at room temperature, or CD8-PE (1:300 Biolegend) or CD11b-PE (1:300 Biolegend). Sections were then mounted with mounting medium (Vector Laboratories). $CD31^+$ vessels, $CD8^+$ cells, and $CD11b^+$ cells were quantified in the regenerating area across six TA muscle samples/groups. Images were captured using a Leica DMI4000 B inverted microscope.

Data analysis and statistics

Statistical analyses were performed using GraphPad Prism (San Diego, USA). Differences between groups were assessed with analysis of variance (ANOVA), followed by Tukey’s post hoc test. A two-tailed, unpaired Student’s t-test was used to compare the two groups. A p-value less than 0.05 ($p<0.05$) was considered statistically significant. Data are presented as means ± standard deviation (SD).

CRediT authorship contribution statement

Shudong Zhao: Writing – review & editing, Writing – original draft, Investigation, Data curation. Lei Wu: Methodology, Investigation, Visualization. Sara Taiyari: Methodology, Investigation. Huiliang Li: Methodology, Investigation. Jianfei Sun: Methodology, Visualization. Jishizhan Chen: Methodology, Investigation. Wenhui Song: Writing – review & editing, Funding acquisition, Conceptualization. Massimiliano Cerletti: Writing – review & editing, Supervision, Funding acquisition, Conceptualization.

Declaration of competing interest

The authors declare no competing financial interest.

Acknowledgments

The authors thank Prof. M. Birchall for his valuable insights on the manuscript. The illustrations in the figures were created using BioRender.com. Funding: This work was supported by the Engineering and Physical Sciences Research Council (EPSRC) of the United Kingdom (grant No. EP/L020904/1, EP/M026884/1, and EP/R02961X/1) and the Wellcome Trust Strategic Support Scheme.

Data Availability

Data will be made available on request.

References

1. Mauro, A., *Satellite cell of skeletal muscle fibers.* J Biophys Biochem Cytol, 1961. **9**(2): p. 493–5.
2. Yin, H., F. Price, and M.A. Rudnicki, *Satellite cells and the muscle stem cell niche.* Physiol Rev, 2013. **93**(1): p. 23–67.
3. Thomas, K., A.J. Engler, and G.A. Meyer, *Extracellular matrix regulation in the muscle satellite cell niche.* Connect Tissue Res, 2015. **56**(1): p. 1–8.
4. Montarras, D., et al., *Direct isolation of satellite cells for skeletal muscle regeneration.* Science, 2005. **309**(5743): p. 2064 - 2067.
5. Tidball, J.G., *Mechanisms of muscle injury, repair, and regeneration.* Compr Physiol, 2011. **1**(4): p. 2029–62.
6. Shandalov, Y., et al., *An engineered muscle flap for reconstruction of large soft tissue defects.* Proc Natl Acad Sci U S A, 2014. **111**(16): p. 6010–5.
7. Chen, M.C., Y.C. Sun, and Y.H. Chen, *Electrically conductive nanofibers with highly oriented structures and their potential application in skeletal muscle tissue engineering.* Acta Biomater, 2013. **9**(3): p. 5562–72.
8. Golebiowska, A.A., et al., *Decellularized extracellular matrix biomaterials for regenerative therapies: advances, challenges and clinical prospects.* Bioactive Materials, 2024. **32**: p. 98–123.
9. Snyder, Y. and S. Jana, *Strategies for development of decellularized heart valve scaffolds for tissue engineering.* Biomaterials, 2022. **288**: p. 121675.
10. Perniconi, B., et al., *The pro-myogenic environment provided by whole organ scale acellular scaffolds from skeletal muscle.* Biomaterials, 2011. **32**(31): p. 7870–82.
11. Urciuolo, A., et al., *Decellularised skeletal muscles allow functional muscle regeneration by promoting host cell migration.* Sci Rep, 2018. **8**(1): p. 8398.
12. Philips, C., L. Terrie, and L. Thorrez, *Decellularized skeletal muscle: A versatile biomaterial in tissue engineering and regenerative medicine.* Biomaterials, 2022. **283**: p. 121436.
13. Garg, K., et al., *Transplantation of devitalized muscle scaffolds is insufficient for appreciable de novo muscle fiber regeneration after volumetric muscle loss injury.* Cell Tissue Res, 2014. **358**(3): p. 857–73.
14. Corona, B.T. and S.M. Greising, *Challenges to acellular biological scaffold mediated skeletal muscle tissue regeneration.* Biomaterials, 2016. **104**: p. 238–46.
15. Smith, A.S., et al., *Characterization and optimization of a simple, repeatable system for the long term in vitro culture of aligned myotubes in 3D.* J Cell Biochem, 2012. **113**(3): p. 1044–53.
16. Trujillo, S., et al., *Engineered Full-Length Fibronectin-Hyaluronic Acid Hydrogels for Stem Cell Engineering.* Adv Healthc Mater, 2020. **9**(21): p. e2000989.
17. Highley, C.B., G.D. Prestwich, and J.A. Burdick, *Recent advances in hyaluronic acid hydrogels for biomedical applications.* Curr Opin Biotechnol, 2016. **40**: p. 35–40.
18. Zhao, W., et al., *Diaphragmatic muscle reconstruction with an aligned electrospun poly(epsilon-caprolactone)/collagen hybrid scaffold.* Biomaterials, 2013. **34**(33): p. 8235–40.
19. Kim, W., M. Kim, and G.H. Kim, *3D - Printed Biomimetic Scaffold Simulating Microfibril Muscle Structure.* Advanced Functional Materials, 2018. **28**(26).
20. Bittner, S.M., et al., *Fabrication and mechanical characterization of 3D printed vertical uniform and gradient scaffolds for bone and osteochondral tissue engineering.* Acta Biomater, 2019. **90**: p. 37–48.

21. Qiao, Z., et al., *Bioinspired stratified electrowritten fiber-reinforced hydrogel constructs with layer-specific induction capacity for functional osteochondral regeneration.* Biomaterials, 2021. **266**: p. 120385.
22. Li, L., et al., *3D Molecularly Functionalized Cell‐Free Biomimetic Scaffolds for Osteochondral Regeneration.* Advanced Functional Materials, 2018. **29**(6).
23. Wagers, A.J., *The stem cell niche in regenerative medicine.* Cell Stem Cell, 2012. **10**(4): p. 362–9.
24. Evano, B. and S. Tajbakhsh, *Skeletal muscle stem cells in comfort and stress.* NPJ Regen Med, 2018. **3**: p. 24.
25. Relaix, F., et al., *Perspectives on skeletal muscle stem cells.* Nat Commun, 2021. **12**(1): p. 692.
26. Limongi, T. and A. Giugni, *Fabrication, Mercury Intrusion Porosimetry Characterization and In Vitro Qualitative Analysis of Biocompatibility of Various Porosities Polycaprolactone Scaffolds.* Journal of Tissue Science & Engineering, 2015. **06**(03).
27. Gillies, A.R. and R.L. Lieber, *Structure and function of the skeletal muscle extracellular matrix.* Muscle Nerve, 2011. **44**(3): p. 318–31.
28. Wilson, K., et al., *The characterization of decellularized human skeletal muscle as a blueprint for mimetic scaffolds.* J Mater Sci Mater Med, 2016. **27**(8): p. 125.
29. Kang, H.W., et al., *A 3D bioprinting system to produce human-scale tissue constructs with structural integrity.* Nat Biotechnol, 2016. **34**(3): p. 312–9.
30. Yang, X., et al., *Appropriate density of PCL nano-fiber sheath promoted muscular remodeling of PGS/PCL grafts in arterial circulation.* Biomaterials, 2016. **88**: p. 34–47.
31. Vannozzi, L., et al., *3D porous polyurethanes featured by different mechanical properties: Characterization and interaction with skeletal muscle cells.* Journal of the mechanical behavior of biomedical materials, 2017. **75**: p. 147–159.
32. García‐Lizarribar, A., et al., *Composite biomaterials as long‐lasting scaffolds for 3D bioprinting of highly aligned muscle tissue.* Macromolecular bioscience, 2018. **18**(10): p. 1800167.
33. Gilbert-Honick, J., et al., *Engineering functional and histological regeneration of vascularized skeletal muscle.* Biomaterials, 2018. **164**: p. 70–79.
34. Xu, Y., et al., *Melatonin‐based and biomimetic scaffold as muscle–ECM implant for guiding myogenic differentiation of volumetric muscle loss.* Advanced Functional Materials, 2020. **30**(27): p. 2002378.
35. Jin, Y., et al., *Functional Skeletal Muscle Regeneration with Thermally Drawn Porous Fibers and Reprogrammed Muscle Progenitors for Volumetric Muscle Injury.* Adv Mater, 2021. **33**(14): p. e2007946.
36. Pei, M., H. Hwangbo, and G. Kim, *Hierarchical fibrous collagen/poly (ε-caprolactone) structure fabricated with a 3D-printing process for tissue engineering applications.* Composites Part B: Engineering, 2023. **259**: p. 110730.
37. Chen, Z., et al., *Influence of the pore size and porosity of selective laser melted Ti6Al4V ELI porous scaffold on cell proliferation, osteogenesis and bone ingrowth.* Mater Sci Eng C Mater Biol Appl, 2020. **106**: p. 110289.
38. Hou, Y., et al., *Surface Roughness Gradients Reveal Topography-Specific Mechanosensitive Responses in Human Mesenchymal Stem Cells.* Small, 2020. **16**(10): p. e1905422.
39. Huang, A., et al., *Fabrication of poly(ε-caprolactone) tissue engineering scaffolds with fibrillated and interconnected pores utilizing microcellular injection molding and polymer leaching.* RSC Advances, 2017. **7**(69): p. 43432–43444.
40. Shao, X., et al., *MatrisomeDB 2.0: 2023 updates to the ECM-protein knowledge database.* Nucleic acids research, 2023. **51**(D1): p. D1519–D1530.

41. Baghdadi, M.B., et al., *Reciprocal signalling by Notch-Collagen V-CALCR retains muscle stem cells in their niche.* Nature, 2018. **557**(7707): p. 714–718.
42. Urciuolo, A., et al., *Collagen VI regulates satellite cell self-renewal and muscle regeneration.* Nat Commun, 2013. **4**: p. 1964.
43. Yao, Y., et al., *Laminin regulates PDGFRbeta(+) cell stemness and muscle development.* Nat Commun, 2016. **7**: p. 11415.
44. Rayagiri, S.S., et al., *Basal lamina remodeling at the skeletal muscle stem cell niche mediates stem cell self-renewal.* Nat Commun, 2018. **9**(1): p. 1075.
45. Ishii, K., et al., *Recapitulation of Extracellular LAMININ Environment Maintains Stemness of Satellite Cells In Vitro.* Stem Cell Reports, 2018. **10**(2): p. 568–582.
46. Lukjanenko, L., et al., *Loss of fibronectin from the aged stem cell niche affects the regenerative capacity of skeletal muscle in mice.* Nat Med, 2016. **22**(8): p. 897–905.
47. Fallon, J.R. and E.M. McNally, *Non-Glycanated Biglycan and LTBP4: Leveraging the extracellular matrix for Duchenne Muscular Dystrophy therapeutics.* Matrix Biol, 2018. **68-69**: p. 616–627.
48. Fukushima, K., et al., *The use of an antifibrosis agent to improve muscle recovery after laceration.* The American journal of sports medicine, 2001. **29**(4): p. 394–402.
49. Lee, E.J., et al., *Fibromodulin: a master regulator of myostatin controlling progression of satellite cells through a myogenic program.* FASEB J, 2016. **30**(8): p. 2708–19.
50. Cho, H.J., et al., *Lumican, an Exerkine, Protects against Skeletal Muscle Loss.* Int J Mol Sci, 2022. **23**(17).
51. Bareja, A., et al., *Liver-derived plasminogen mediates muscle stem cell expansion during caloric restriction through the plasminogen receptor Plg-R(KT).* Cell Rep, 2024. **43**(3): p. 113881.
52. McArthur, S., et al., *Annexin A1 drives macrophage skewing to accelerate muscle regeneration through AMPK activation.* J Clin Invest, 2020. **130**(3): p. 1156–1167.
53. Defour, A., et al., *Annexin A2 links poor myofiber repair with inflammation and adipogenic replacement of the injured muscle.* Hum Mol Genet, 2017. **26**(11): p. 1979–1991.
54. Demonbreun, A.R., et al., *Recombinant annexin A6 promotes membrane repair and protects against muscle injury.* J Clin Invest, 2019. **129**(11): p. 4657–4670.
55. Olguin, H.C., et al., *Reciprocal inhibition between Pax7 and muscle regulatory factors modulates myogenic cell fate determination.* The Journal of cell biology, 2007. **177**(5): p. 769–779.
56. Loh, Q.L. and C. Choong, *Three-dimensional scaffolds for tissue engineering applications: role of porosity and pore size.* Tissue Eng Part B Rev, 2013. **19**(6): p. 485–502.
57. Deasy, B.M., R.J. Jankowski, and J. Huard, *Muscle-derived stem cells: characterization and potential for cell-mediated therapy.* Blood Cells Mol Dis, 2001. **27**(5): p. 924–33.
58. Usas, A. and J. Huard, *Muscle-derived stem cells for tissue engineering and regenerative therapy.* Biomaterials, 2007. **28**(36): p. 5401–6.
59. Cao, B. and J. Huard, *Muscle-derived stem cells.* Cell Cycle, 2004. **3**(2): p. 101–104.
60. Huard, J., *Regenerative medicine based on muscle stem cells*. 2008, Wiley Online Library.
61. Yeo, M. and G.H. Kim, *Anisotropically Aligned Cell-Laden Nanofibrous Bundle Fabricated via Cell Electrospinning to Regenerate Skeletal Muscle Tissue.* Small, 2018. **14**(48): p. e1803491.
62. Perez-Puyana, V., et al., *Fabrication of hybrid scaffolds obtained from combinations of PCL with gelatin or collagen via electrospinning for skeletal muscle tissue engineering.* J Biomed Mater Res A, 2021. **109**(9): p. 1600–1612.

63. Pham-Nguyen, O.V., et al., *Preparation of Stretchable Nanofibrous Sheets with Sacrificial Coaxial Electrospinning for Treatment of Traumatic Muscle Injury.* Adv Healthc Mater, 2021. **10**(8): p. e2002228.
64. Choi, J.S., et al., *The influence of electrospun aligned poly(epsilon-caprolactone)/collagen nanofiber meshes on the formation of self-aligned skeletal muscle myotubes.* Biomaterials, 2008. **29**(19): p. 2899–906.
65. Khorshidi, S., et al., *A review of key challenges of electrospun scaffolds for tissue-engineering applications.* J Tissue Eng Regen Med, 2016. **10**(9): p. 715–38.
66. Shahriari, D., et al., *Scalable Fabrication of Porous Microchannel Nerve Guidance Scaffolds with Complex Geometries.* Adv Mater, 2019. **31**(30): p. e1902021.
67. Sampath, S.C., et al., *Induction of muscle stem cell quiescence by the secreted niche factor Oncostatin M.* Nature Communications, 2018. **9**(1).
68. Wang, Z., et al., *Fibronectin type III domain-containing 4 promotes the migration and differentiation of bovine skeletal muscle-derived satellite cells via focal adhesion kinase.* Cell Adh Migr, 2020. **14**(1): p. 153–164.
69. Engler, A.J., et al., *Matrix elasticity directs stem cell lineage specification.* Cell, 2006. **126**(4): p. 677–89.
70. Gribova, V., et al., *Effect of RGD functionalization and stiffness modulation of polyelectrolyte multilayer films on muscle cell differentiation.* Acta Biomater, 2013. **9**(5): p. 6468–80.
71. Gilbert, P.M., et al., *Substrate elasticity regulates skeletal muscle stem cell self-renewal in culture.* Science, 2010. **329**(5995): p. 1078–81.
72. Madl, C.M., S.C. Heilshorn, and H.M. Blau, *Bioengineering strategies to accelerate stem cell therapeutics.* Nature, 2018. **557**(7705): p. 335–342.
73. Asano, T., et al., *Optogenetic induction of contractile ability in immature C2C12 myotubes.* Sci Rep, 2015. **5**: p. 8317.
74. Cheesbrough, A., et al., *A scalable human iPSC-based neuromuscular disease model on suspended biobased elastomer nanofiber scaffolds.* Biofabrication, 2023. **15**(4).
75. Sebille, S., et al., *Optogenetic approach for targeted activation of global calcium transients in differentiated C2C12 myotubes.* Sci Rep, 2017. **7**(1): p. 11108.
76. Cheesbrough, A., et al., *Biobased Elastomer Nanofibers Guide Light-Controlled Human-iPSC-Derived Skeletal Myofibers.* Adv Mater, 2022. **34**(18): p. e2110441.
77. Urciuolo, A. and P. De Coppi, *Decellularized Tissue for Muscle Regeneration.* Int J Mol Sci, 2018. **19**(8).
78. Sherwood, R.I., et al., *Isolation of adult mouse myogenic progenitors: functional heterogeneity of cells within and engrafting skeletal muscle.* Cell, 2004. **119**(4): p. 543–54.
79. Cerletti, M., et al., *Highly efficient, functional engraftment of skeletal muscle stem cells in dystrophic muscles.* Cell, 2008. **134**(1): p. 37–47.
80. Cerletti, M., et al., *Short-term calorie restriction enhances skeletal muscle stem cell function.* Cell Stem Cell, 2012. **10**(5): p. 515–9.

Figures and legends

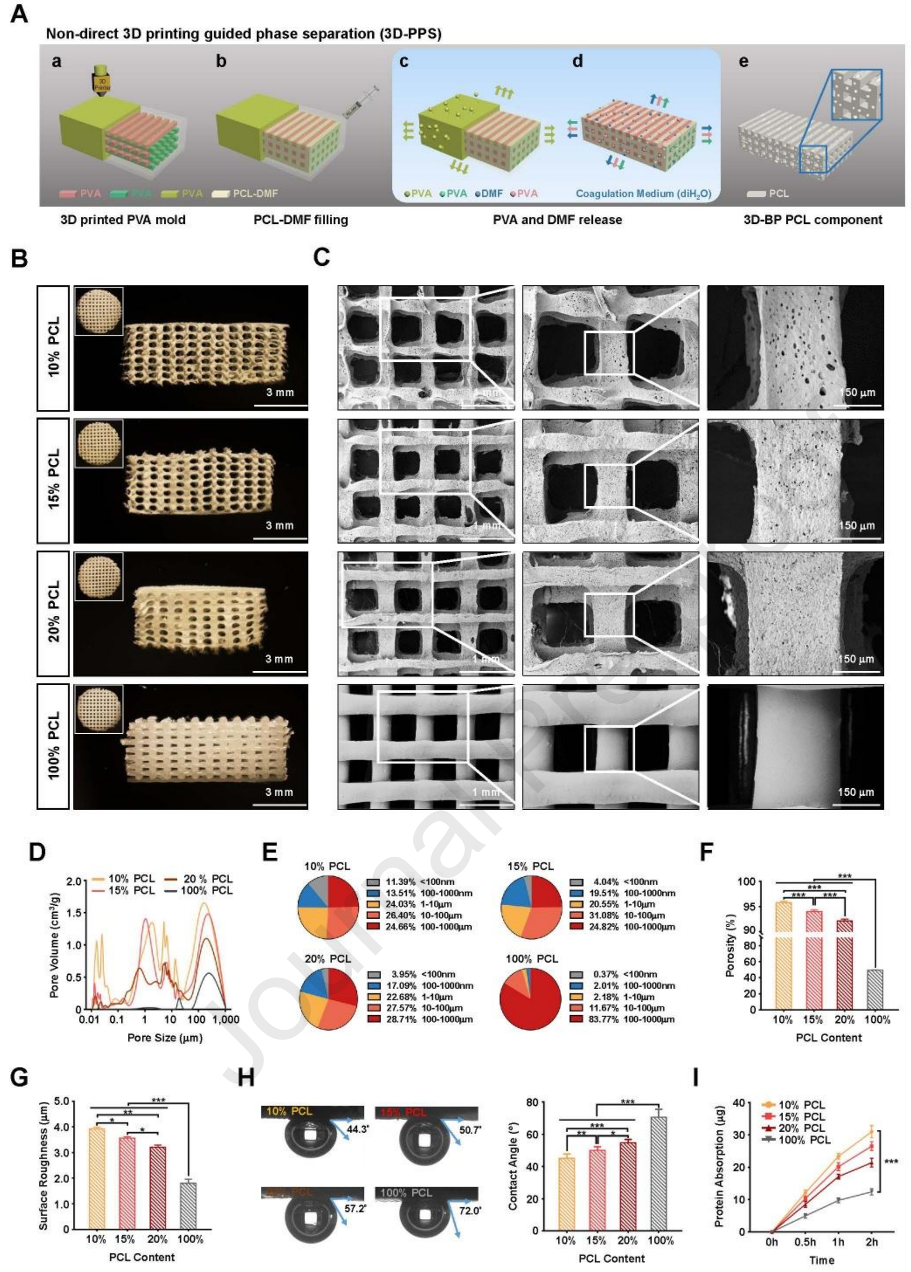

Fig. 1. Fabrication and characterization of 3D-BPs. (**A**) Experimental process for creating 3D-BPs: a. Digitally designing and printing the 3D PVA mold. b. Filling the 3D PVA mold with PCL-DMF. c-d. Dissolving the PCL and DMF. e. Producing the 3D-BP. (**B-C**) Optical (left) and SEM (right) images showing the structure and surface morphology of 3D-BPs with 10%, 15%, and 20% PCL, as well as 100% PCL (scale bars: 150 µm – 3 mm). (**D-I**) Characterization of 3D-BPs includes measurements of pore volume, pore size distribution, porosity, surface roughness, contact angle, and protein absorption (10% PCL in yellow, 15% PCL in red, 20% PCL in dark red) and 100% PCL (in gray). *p<0.05, **p<0.01, ***p<0.001.

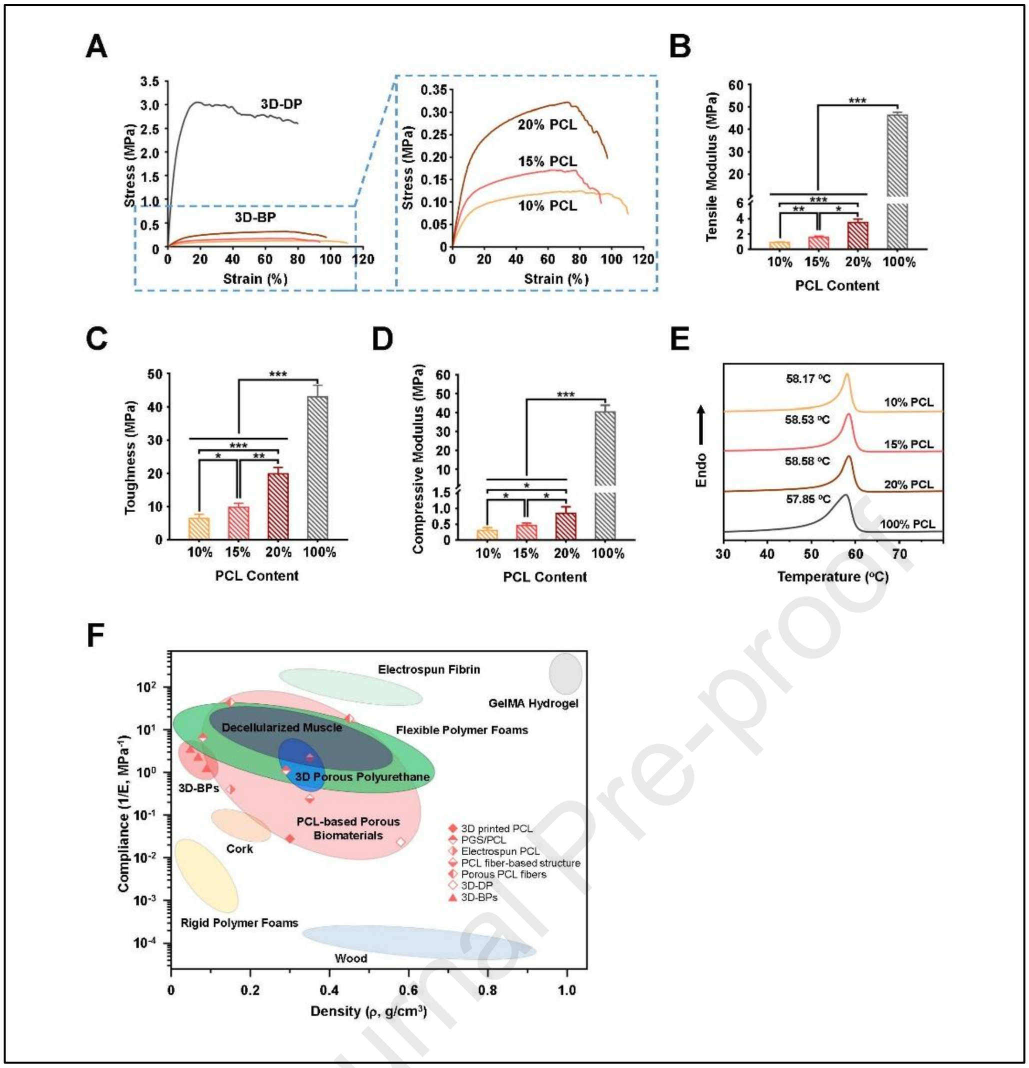

Fig. 2. The physical and mechanical properties of 3D-BPs. (**A-E**) The tensile modulus, toughness, compressive modulus, and crystallinity of 3D-BPs (10% PCL in yellow, 15% PCL in red, and 20% PCL in dark red) are shown alongside 100% PCL in gray. (**F**) An Ashby plot compares compliance and density for 3D-BPs and various other porous natural and synthetic materials, including wood, cork, flexible polymer foams, decellularized muscle, PCL-based porous biomaterials, electrospun fibrin, GelMA hydrogel, 3D porous polyurethane, and rigid polymer foams. $*p<0.05$, $**p<0.01$, $***p<0.001$.

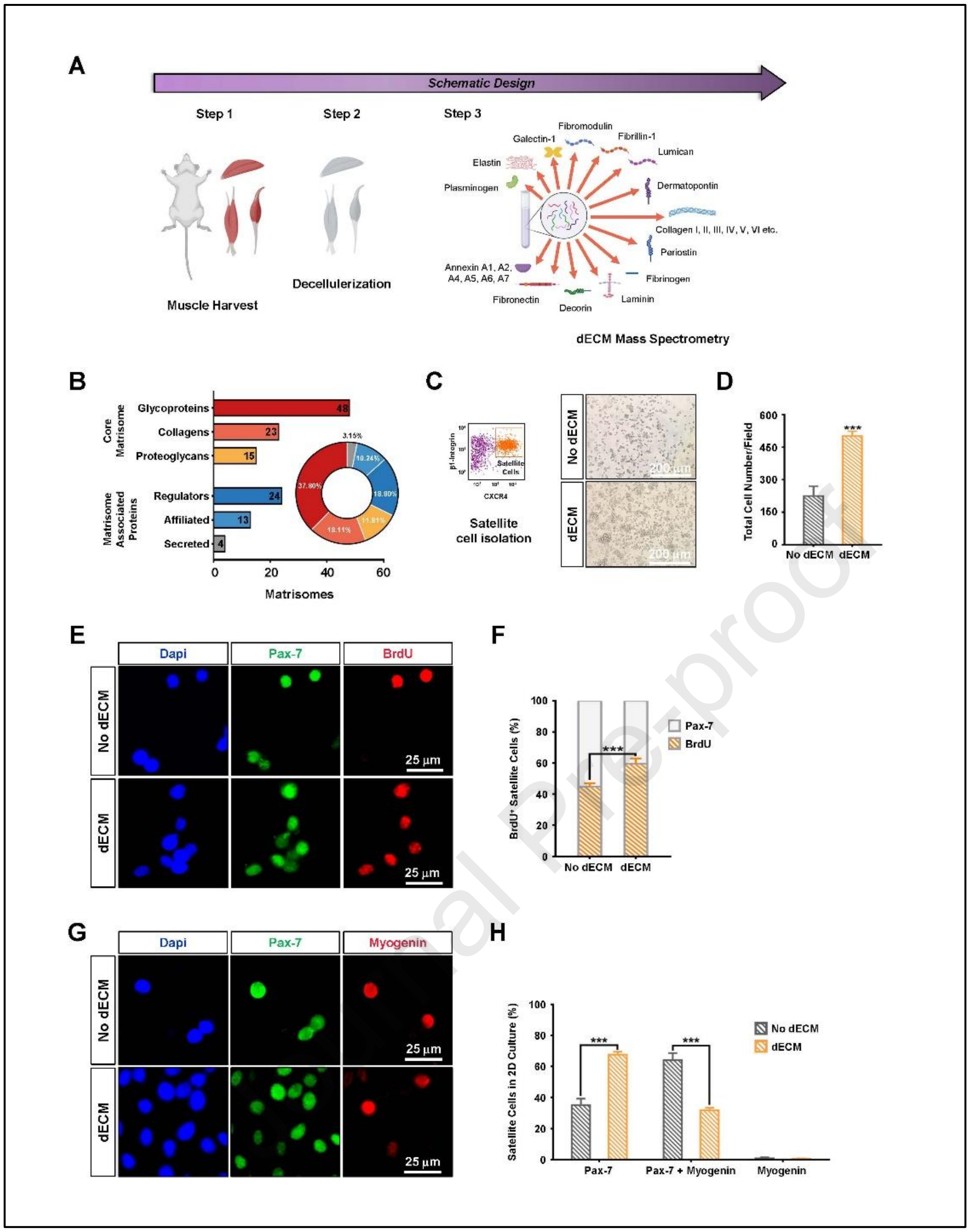

Fig. 3. Composition of muscle dECM hydrogel and its role in regulating muscle satellite cells. (**A**) Experimental design: harvesting limb muscles, decellularization, and analyzing dECM hydrogel via mass spectrometry. (**B**) Characterization and classification of dECM hydrogel proteins. (**C-D**) FACS plot shows the satellite cell isolation profile and includes optical images of satellite cells five days after seeding in dECM hydrogel-functionalized plates and no-dECM control plates. Bar graphs depict the total cell count per field. (**E-F**) Images of BrdU$^+$ muscle satellite cells in dECM hydrogel cultures. Pax-7$^+$ satellite cells are stained green; BrdU$^+$ cells are red; nuclei are blue. Bar graphs show the percentage of BrdU$^+$ satellite cells. (**G-H**) Images of myogenin$^+$ cells in dECM hydrogel cultures. Pax-7$^+$ satellite cells are stained green; myogenin$^+$ cells are red; nuclei are blue. Bar graphs display the percentages of Pax-7$^+$, Pax-7$^+$/myogenin$^+$, and myogenin$^+$ cells (scale bars: 25 µm). ***$p<0.001$.

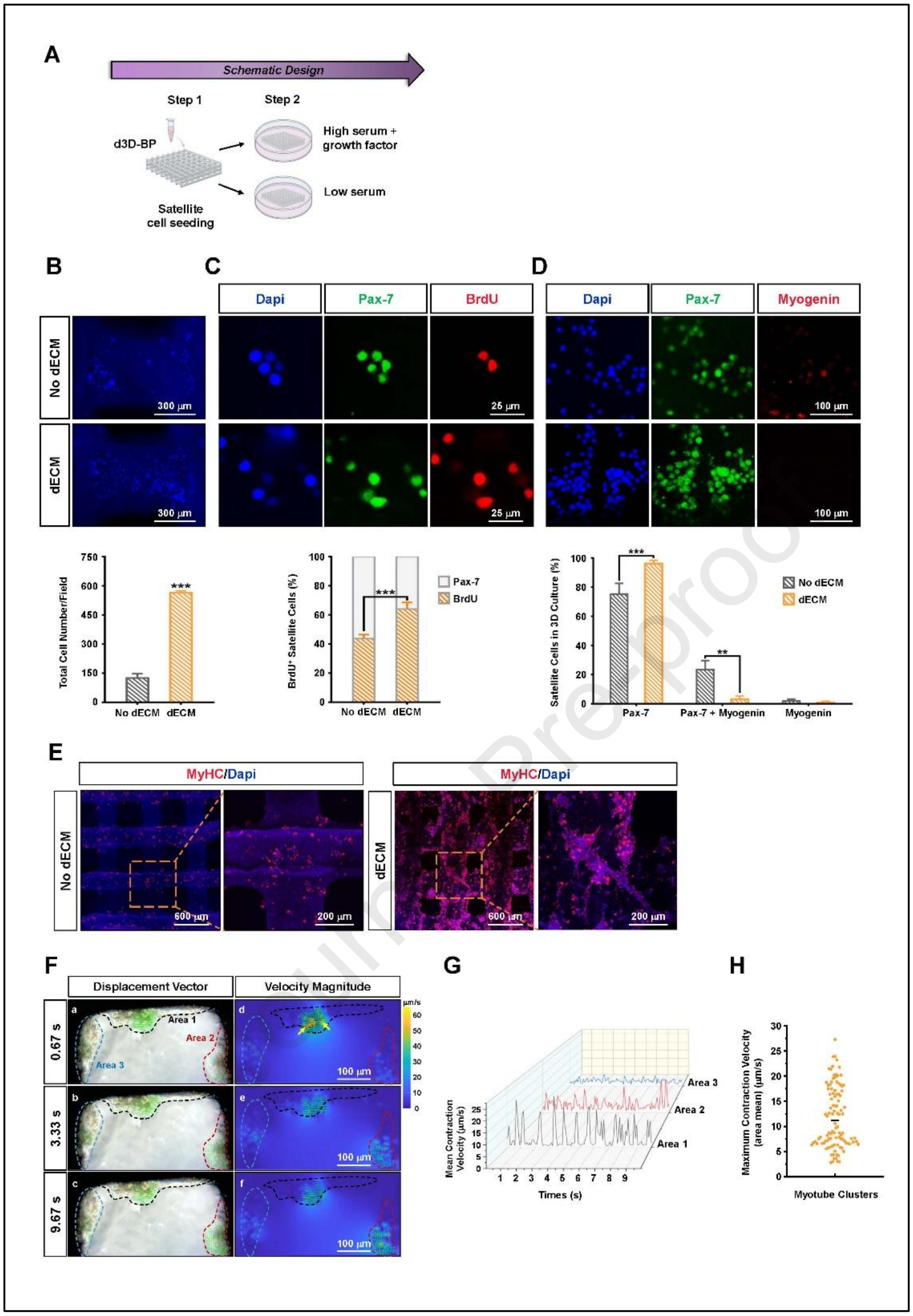

Fig. 4. d3D-BP enhances satellite cell maintenance and promotes the formation of twitching myotubes. (**A**) Experimental setup: culturing muscle satellite cells in d3D-BPs with either high or low serum levels for expansion and differentiation. (**B**) Images of satellite cells in d3D-BPs on day 5 after seeding (nuclei stained blue with DAPI). Bar graphs show the total cell count per field. (**C**) Images of BrdU$^+$ satellite cells in d3D-BPs. Pax-7$^+$ satellite cells are stained green, BrdU$^+$ cells are red, and nuclei are blue. Bar graphs depict the percentage of BrdU$^+$ satellite cells. (**D**) Images of myogenin$^+$ cells in d3D-BPs. Pax-7$^+$ satellite cells are stained green, myogenin$^+$ cells are red, and nuclei are blue. Bar graphs display the percentages of Pax-7$^+$, Pax-7$^+$/myogenin$^+$, and myogenin$^+$ cells (scale bars: 25-300 μm). (**E**) Representative images of myotubes derived from satellite cells in d3D-BPs on day 14 in differentiation medium showing MyHC$^+$ myoblasts and myotubes stained red, with nuclei appearing blue (scale bars: 200-600 μm). (**F**) Particle image velocimetry (PIV) vector plots and velocity magnitude heat maps of spontaneous contractions at peak contraction

recorded at three time points: 0.67 s, 3.33 s, and 9.67 s (a-f). (**G**) Variation in mean contraction velocity across each myofiber cluster area is shown over a 10-second period. (**H**) Peak contraction velocities within each myofiber cluster are displayed over a 10-second interval. **p<0.01, ***p<0.001.

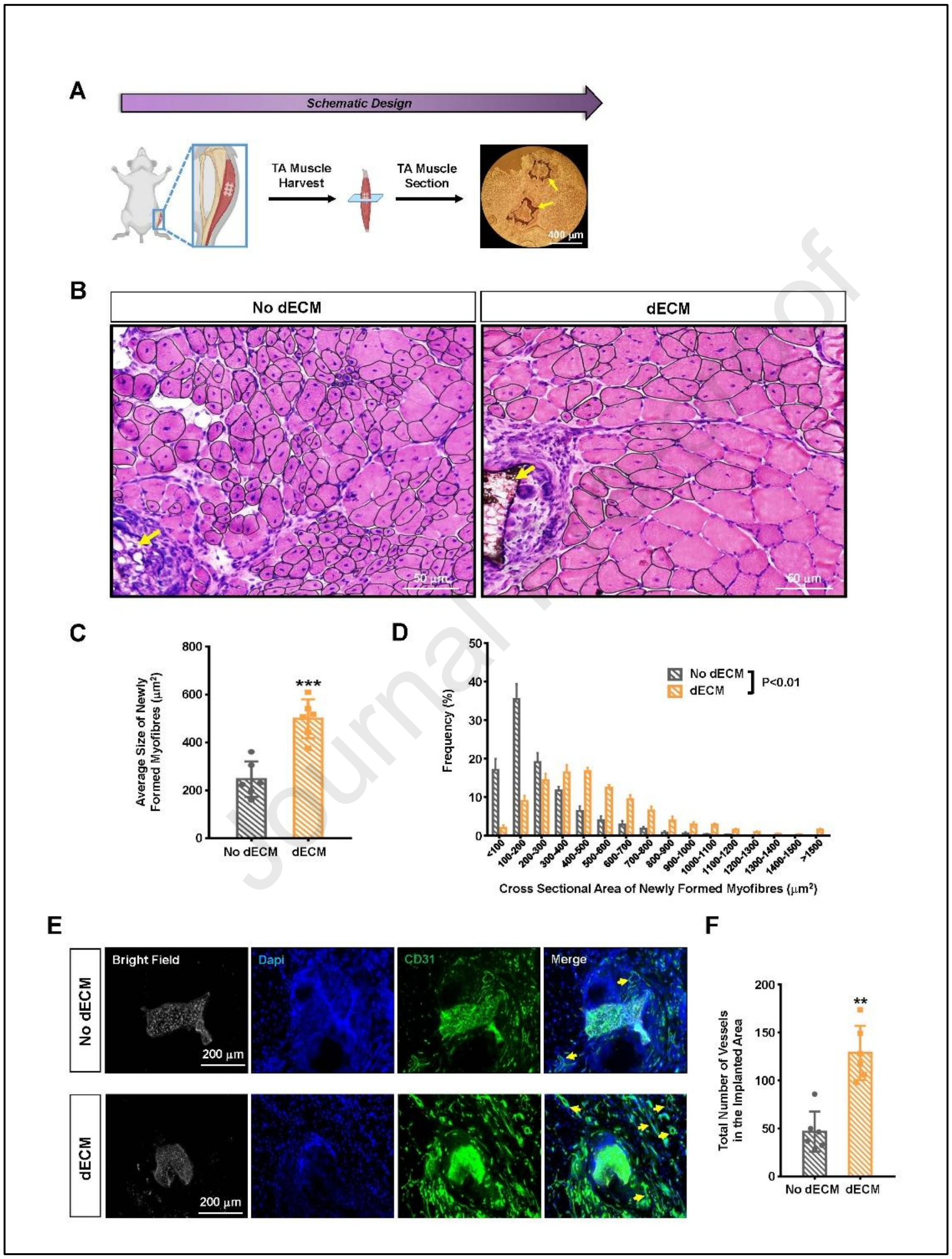

Fig. 5. d3D-BP promotes myofiber regeneration and blood vessel formation. (**A**) A schematic diagram illustrates the implantation and analysis of d3D-BP. d3D-BP constructs and 3D-BP controls were implanted into the tibialis anterior (TA) muscles, which were examined after 28 days. Arrows indicate the implantation site within the TA muscle section. (**B**) H&E staining of TA muscles shows newly regenerating, centrally nucleated myofibers in both the d3D-BP and 3D-BP control-implanted areas (yellow arrows indicate the biomaterial location). (**C-D**) The quantification and size distribution of the newly regenerating, centrally nucleated myofibers are presented (yellow bars). (**E-F**) Images display blood vessels in the d3D-BP and 3D-BP control-implanted regions of

TA muscle sections. Blood vessels are stained with CD31 (green), and nuclei are stained with DAPI (blue). Bar graphs show the total number of blood vessels. $^{**}p<0.01$, $^{***}p<0.001$.

Declaration of interests

☒ The authors declare that they have no known competing financial interests or personal relationships that could have appeared to influence the work reported in this paper.

☐ The authors declare the following financial interests/personal relationships which may be considered as potential competing interests: